

RESEARCH

Open Access



Flexural Performance of Steel Reinforced ECC-Concrete Composite Beams Subjected to Freeze–Thaw Cycles

Wenjie Ge^{1,2*} , Ashraf F. Ashour³, Weigang Lu² and Dafu Cao¹

Abstract

Experimental and theoretical investigations on the flexural performance of steel reinforced ECC-concrete composite beams subjected to freeze–thaw cycles are presented in this paper. Four groups of reinforced composite beams with different ECC height replacement ratios subject to 0, 50, 100 and 150 cycles of freeze–thaw were physically tested to failure. Experimental results show that the bending capacity decreases with the increase of freeze–thaw cycles regardless of ECC height replacement ratios. However, the ultimate moment, stiffness and durability of ECC specimens and ECC-concrete composite specimens are greater than those of traditional concrete specimens, owing to the excellent tensile performance of ECC materials. With the increase of ECC height, the crack width and average crack spacing gradually decrease. According to materials' constitutive models, compatibility and equilibrium conditions, three failure modes with two boundary failure conditions are proposed. Simplified formulas for the moment capacity are also developed. The results predicted by the simplified formulas show good agreement with the experimental moment capacity and failure modes. A parametric analysis is conducted to study the influence of strength and height of ECC, amount of reinforcement, concrete strength and cycles of freeze–thaw on moment capacity and curvature ductility of ECC-concrete composite beams.

Keywords: freeze–thaw cycles, ECC, concrete, composite beams, flexural performance

1 Introduction

Many structures are subjected to harsh environment in the cold regions of the world, for example northern Europe, Canada, Russian, northeast Asia, causing partial or full damage due to freeze–thaw severe environment. Engineered cementitious composite (ECC) has been successfully used in many structures as it has excellent tensile performance and exhibits multiple micro cracks, resulting in a greatly improvement of strain capacity, toughness, ductile performance and energy dissipation ability (Li et al. 2001; Li 2012; Yoo and Yoon 2016; Kang et al. 2016; Smarzewski and Barnat-Hunek 2017). ECC

has also shown self-healing capability (Liu et al. 2017; Hung and Su 2016), excellent freeze–thaw resistance ability (Yun et al. 2011; Ge et al. 2018; Özbay et al. 2013), fire-resistance ability (Wu and Li 2017; Pourfalah 2018) and durability in severe environment (Liu et al. 2017; Özbay et al. 2013).

Experimental investigations show that replacement of concrete with ECC material has improved both the bending capacity (Zhang 2014; Zhang et al. 2017; Wu et al. 2017; Ding et al. 2018; Ge et al. 2018) and ductility (Zhang et al. 2017; Wu et al. 2017; Ding et al. 2018; Ge et al. 2018), but, also significantly reduced the crack width especially before yielding of steel (Pourfalah 2018). Consequently, waterproof and corrosion resistance (Maalej and Li 1995; Maalej and Leong 2005; Maalej et al. 2012) are also enhanced, resulting in durability improvement of ECC-concrete composite components.

*Correspondence: gewej@yzu.edu.cn

¹ College of Civil Science and Engineering, Yangzhou University, Yangzhou 225127, China

Full list of author information is available at the end of the article
Journal information: ISSN 1976-0485 / eISSN 2234-1315

Many research studies have focused on investigating various properties of reinforced concrete beams exposed to freeze–thaw cycling. For example, acoustic emission activity of CFRP-strengthened reinforced concrete beams (Choi and Yun 2015), steel reinforced/prestressed concrete beams (Cao et al. 2015, 2016; Qin et al. 2016), the effect of subfreezing temperatures on the behavior and ultimate capacity of GFRP-reinforced concrete beams (Berry et al. 2017) and the flexural performance of reinforced concrete beams subjected to the coupling action of freeze–thaw cycles and sustained loading in mixed aggressive environment (Diao et al. 2009). On the other hand, investigations on the flexural performance of steel reinforced ECC-concrete elements in severe environment, including freeze–thaw cycling, are relatively limited.

In this paper, experimental and analytical studies are conducted to evaluate the effect of freeze–thaw cycles on deflections, cracks, bending capacity and failure modes of

ECC-concrete composite beams. Based on the analytical investigation developed, three failure modes, two boundary failure conditions and their discriminant are proposed. A comprehensive parametric study is also conducted, considering the effect of strength and amount of reinforcement, concrete strength, ECC strength and height on flexural performance of composite beams after freeze–thaw cycles.

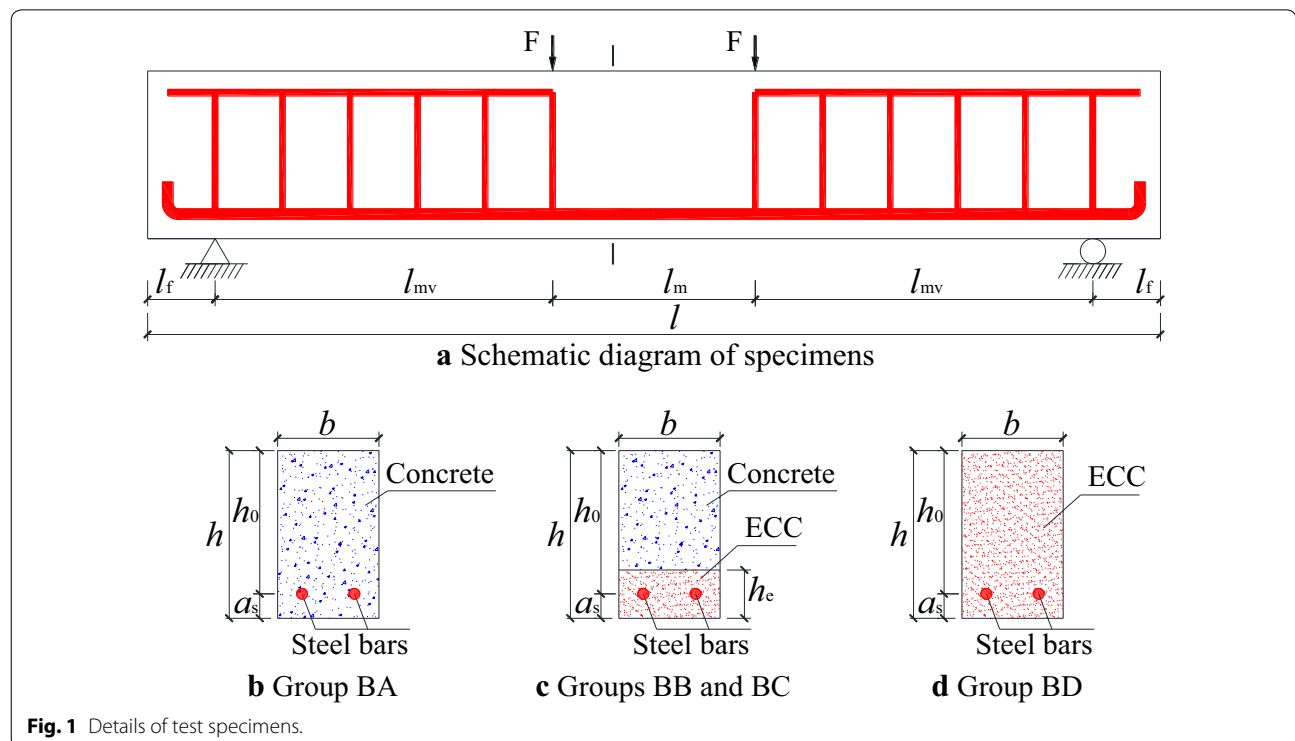
2 Experimental Program

2.1 Test Specimens Design

Table 1 lists the sixteen beams and the values of the two main parameters considered in this investigation, namely the ECC height replacement ratio, r_h and number of freeze–thaw cycles, n . Fig 1 shows the geometrical dimensions, reinforcement, materials used and supporting system test specimens. The specimen total span length $l=1000$ mm, flexural-shear span length $l_{mv}=300$ mm, pure flexural span length $l_m=300$ mm. Cross-section width b and height h are 100 and 150 mm,

Table 1 Specimen design parameters.

Notation	r_h	n									
BA-0	0	0	BB-0	0.3	0	BC-0	0.6	0	BD-0	1.2	0
BA-50	0	50	BB-50	0.3	50	BC-50	0.6	50	BD-50	1.2	50
BA-100	0	100	BB-100	0.3	100	BC-100	0.6	100	BD-100	1.2	100
BA-150	0	150	BB-150	0.3	150	BC-150	0.6	150	BD-150	1.2	150



respectively, the vertical distance of the cross-section bottom edge to the centroid of steel bars a_s is 25 mm, the cross-section effective height h_0 is 125 mm. The top steel reinforcement is $2\phi 10$, h_e is the ECC replacement height and r_h is the ECC height replacement ratio, $r_h = h_e/h_0$. The bottom longitudinal reinforcement is $2\phi 12$ for all test specimens. Each group notation is selected to identify the ECC height replacement ratio used (BA, BB, BC and BD represents $r_h = 0, 0.30, 0.60$ and 1.20 , respectively) and the cycles n (0, 50, 100 and 150) of freeze–thaw. All specimens were loaded by two equal point loads and simply supported as shown in Fig. 1.

2.2 Test Instrumentation Layout

Displacement transducers were located at midspan, loading and supporting points to measure movements at these locations. The load was applied by a manual hydraulic jack and measured by a load transducer. Two electrical resistance strain acquisition units (DP3862) were used to capture strains at various stages of loading: one was connected to the load transducer while the other was used to capture strains from mid-span strain gauges attached to steel reinforcement. Equidistant dial indicators installed along the height of the beam cross-section at midspan were used to measure the average ECC/concrete strains. The size of cracks along the span was measured by crack width measurement instrument KON-FK (B) (Zhou 2013).

2.3 Freeze–Thaw Cycles Test

The rapid water freezing and thawing method was adopted (China Renewable Energy Engineering Institute 2006), the maximum and minimum temperatures at the core area of specimens should be controlled at 8 ± 2 °C and -17 ± 2 °C, respectively, and every cycle should be accomplished within 4 h. The freeze–thaw test

system was used to accomplish the required cycles. Once achieved the predetermined cycles, tests of concrete cubes, ECC (flat-plates for tension and prisms for compression), flexural specimens (concrete beams, ECC-concrete composite beams and ECC beams) were conducted as explained below.

2.4 Materials

2.4.1 Concrete

Concrete cubic compressive properties were determined from testing $150 \times 150 \times 150$ mm³ concrete cube specimens (China Academy of Building Research 2003) (three specimens for each group) and are presented in Table 2. f_{cu} is the compressive strength of concrete cube, u and CoV represent the mean and variation coefficient of measured compressive strength, respectively. Compressive strength, tensile strength and modulus of elasticity are calculated in accordance to reference (China Academy of Building Research 2010).

2.4.2 Ecc

Tensile properties presented in Table 3 were obtained from testing three $40 \times 15 \times 160$ mm³ rectangular flat-plates (Ge et al. 2018). u and CoV represent the mean and variation coefficient of measured tensile strength, respectively. ECC compressive properties presented in Table 4 were captured from testing three $40 \times 40 \times 160$ mm³ prismatic specimens (Ge et al. 2018; Xu et al. 2009). f_{ecp} and ε_{ecp} are the stress and strain corresponding to the peak point of curves, respectively. The measured stress–strain curves of ECC are shown in Fig. 2.

2.4.3 Steel reinforcement

Table 5 presents the mechanical properties (General Administration of Quality Supervision, Inspection and

Table 2 Compressive strength of concrete cubes.

Cycles of freeze–thaw	Cubic compressive strength			Compressive strength			Tensile strength			Modulus of elasticity		
	f_{cu} (MPa)	u (MPa)	CoV	f_c (MPa)	u (MPa)	CoV	f_t (MPa)	u (MPa)	CoV	E_c (GPa)	u (MPa)	CoV
0	47.3	47.0	0.011	31.6	31.5	0.014	3.0	3.0	0.009	34.1	34.0	0.003
	47.5			31.8			3.0			34.1		
	46.3			31.0			3.0			33.9		
50	36.3	35.6	0.014	24.3	23.8	0.018	2.5	2.5	0.012	31.7	31.5	0.005
	35.4			23.7			2.5			31.4		
	35.1			23.5			2.5			31.4		
100	31.1	29.8	0.03	20.8	20.0	0.037	2.3	2.2	0.025	30.2	29.7	0.013
	29.3			19.6			2.2			29.5		
	29.1			19.5			2.2			29.5		
150	25.4	26.1	0.021	17.0	17.5	0.025	2.0	2.0	0.017	28.0	28.3	0.010
	26.7			17.9			2.1			28.6		
	26.2			17.5			2.0			28.4		

Table 3 Tensile properties of ECC rectangular flat-plates.

Cycles of freeze–thaw	Tensile strength at first cracking			Tensile strain at first cracking			Ultimate tensile strength			Ultimate tensile strain		
	f_{etc} (MPa)	u (MPa)	CoV	ϵ_{etc} (%)	u (%)	CoV	f_{etu} (MPa)	u (MPa)	CoV	ϵ_{etu} (%)	u (%)	CoV
0	2.04	2.10	0.021	0.023	0.024	0.039	2.41	2.41	0.003	2.50	2.69	0.074
	2.14			0.025			2.40			2.60		
	2.12			0.025			2.42			2.96		
50	1.98	1.92	0.023	0.029	0.027	0.046	2.40	2.30	0.030	3.00	2.90	0.027
	1.87			0.026			2.24			2.81		
	1.92			0.027			2.27			2.90		
100	1.76	1.80	0.016	0.033	0.030	0.072	2.12	2.17	0.019	2.96	3.10	0.032
	1.83			0.028			2.22			3.19		
	1.81			0.029			2.16			3.15		
150	1.74	1.72	0.018	0.03	0.033	0.075	2.05	1.98	0.026	3.26	3.30	0.025
	1.68			0.036			1.96			3.23		
	1.75			0.034			1.93			3.42		

Table 4 Compressive properties of ECC prismatic specimens.

Cycles of freeze–thaw	Compressive strength			Corresponding strain		
	f_{ecp} (MPa)	u (MPa)	CoV	ϵ_{ecp} (%)	u (%)	CoV
0	31.4	31.4	0.010	0.37	0.36	0.023
	31.8			0.35		
	31.0			0.36		
50	30.2	29.9	0.010	0.39	0.39	0.032
	29.5			0.38		
	30.0			0.41		
100	28.8	28.2	0.014	0.43	0.42	0.030
	28.1			0.40		
	27.8			0.42		
150	26.0	25.7	0.015	0.45	0.45	0.028
	25.1			0.44		
	25.9			0.47		

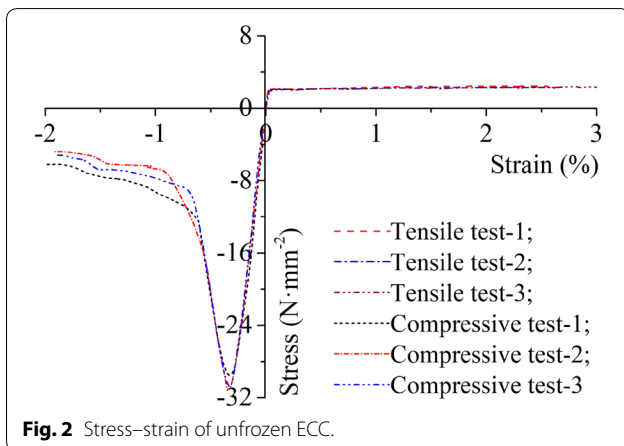


Fig. 2 Stress–strain of unfrozen ECC.

Quarantine of the People’s Republic of China. Metallic materials tensile testing at ambient temperature GB/T228-2002) of steel reinforcements, as the tested freeze–thaw temperature range ($-17 \pm 2 \text{ }^\circ\text{C} - 8 \pm 2 \text{ }^\circ\text{C}$) has less effect (Liu et al. 2008), their values are considered as constant.

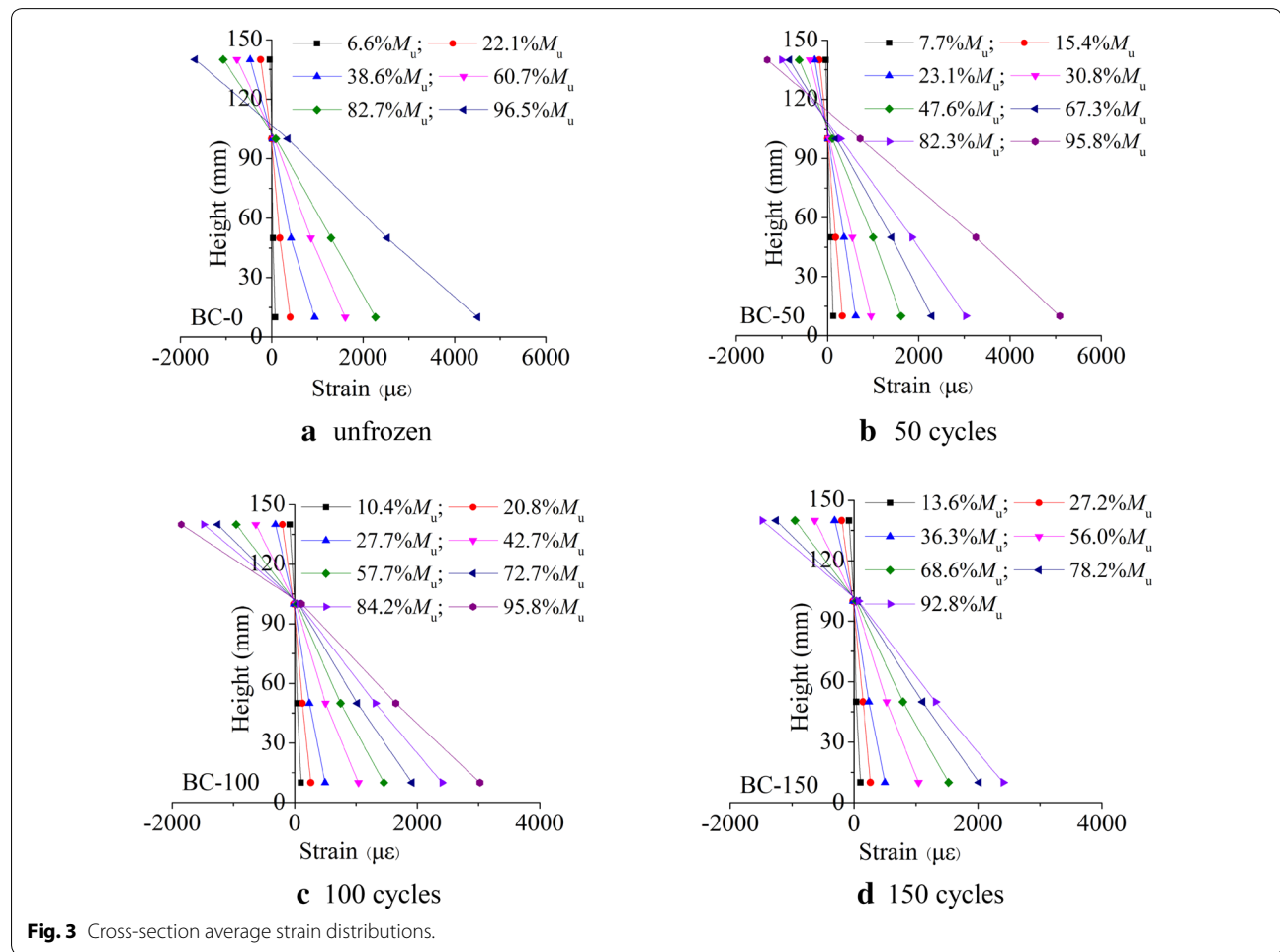
3 Test Results

3.1 Load–Strain Distribution

Figure 3 (taking group BC for example) presents the cross-section average strain distributions at various loads, Fig. 3a–d for 0, 50, 100 and 150 freeze–thaw cycles, respectively.

Table 5 Mechanical properties of reinforcing bars

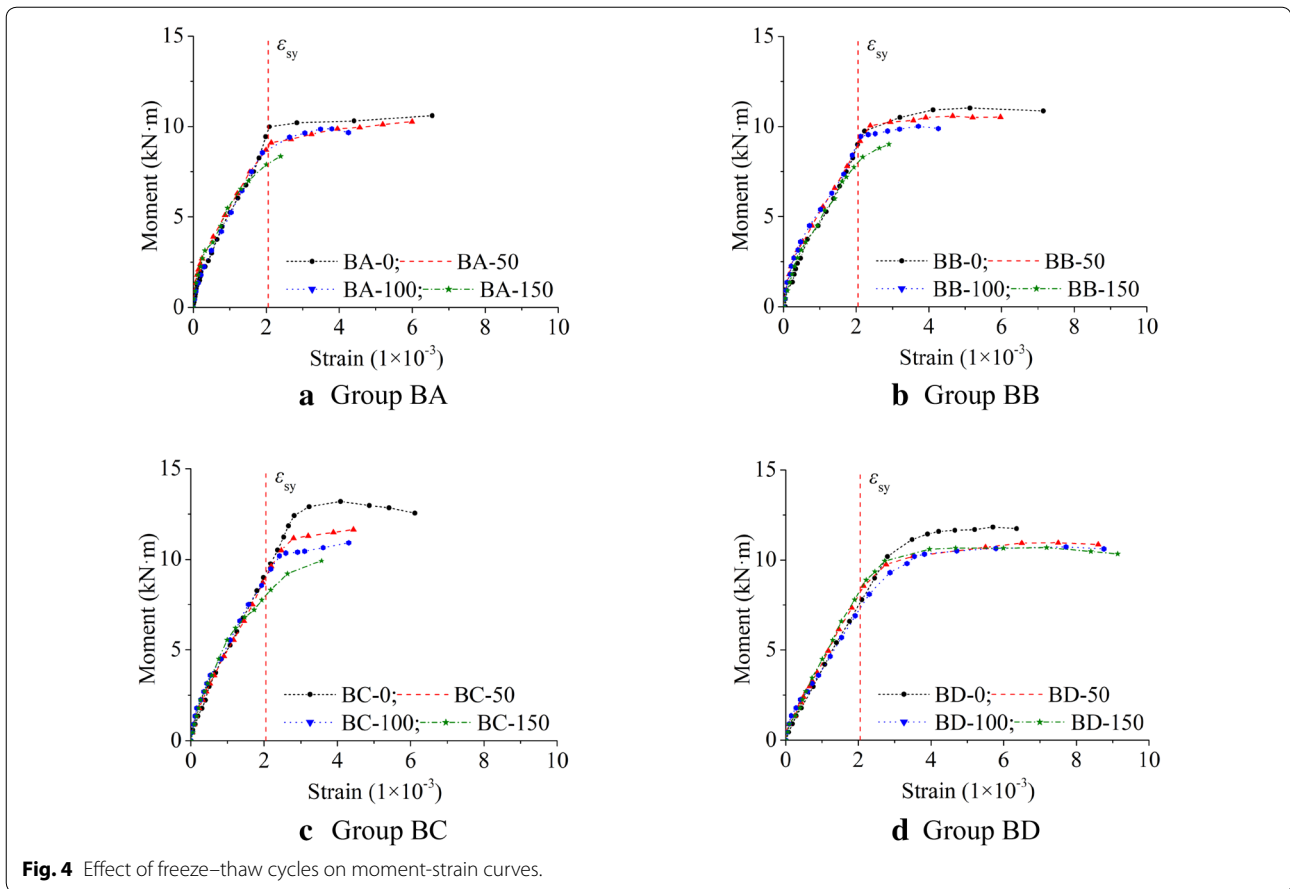
Diameter (mm)	Yield strength			Ultimate strength			Elastic modulus		
	f_y (MPa)	u (MPa)	CoV	f_u (MPa)	u (MPa)	CoV	E_s (GPa)	u (GPa)	CoV
8	410	406	0.009	489	485	0.006	199	198	0.002
	407			482			198		
	401			485			198		
12	407	408	0.003	503	503	0.003	199	199	0.002
	410			501			199		
	408			505			198		



As observed from Fig. 3, the cross-section strain is generally linearly distributed, validating the plane-section assumption and no delamination between concrete and ECC.

Figure 4 presents the specimens midspan moment-steel strain curves. As observed from Fig. 4, the steel bars of all specimens yielded. After yielding of steel reinforcement, the steel strains of group BA (reinforced concrete

specimens) increase, even the load does not increase, indicating full but gradual collapse of test specimens. On the other hand, test specimens in group BD (reinforced ECC specimens), groups BB and BC (reinforced ECC-concrete composite specimens) are able to carry more moments beyond yielding of steel, indicating that ECC materials in tensile zone can provide tensile resistance together with steel bar.



3.2 Midspan Load–Deflection Curves

Figure 5 presents the specimens midspan moment–deflection curves. Relative bending capacity and deflections with respect to control unfrozen reinforced concrete beams are presented in Table 6. M_u is the bending capacity of each specimen, M_{u0} is the bending capacity of control unfrozen specimen in each group. M_{q0} and d_q are the moment and the corresponding deflections under quasi-permanent combinations of unfrozen specimen (BA-0, BB-0, BC-0 and BD-0), respectively.

As observed from Fig. 5 and Table 6, the bending capacities decrease with the increase of freeze–thaw cycles regardless of the cross-section form. After 50, 100 and 150 cycles, the bending capacities of group BA are 97%, 93% and 69% of that of its control unfrozen specimen BA-0, respectively. The ultimate moments of group BB are 96%, 91% and 82% of that of its comparison control unfrozen specimen BB-0, respectively. The ultimate moments of group BC are 86%, 80% and 73% of that of its control unfrozen specimen BC-0 respectively. The ultimate moments of group BD are 93%, 91% and 90%, respectively, of that of its control unfrozen specimen BD-0. Deflections of specimens after 50 and 100 cycles

are generally lower, but after 150 cycles are higher, than that of control unfrozen specimen. This observation is in agreement with a previous investigation (Ge et al. 2018) that showed that the positive effect of water conservation environment on the elastic modulus is greater than the negative effect of freeze–thaw less than 100 cycles.

Table 7 presents the comparisons of bending capacities and deflections, where the reinforced concrete specimens are taken as comparison specimen. M_{uc} is the bending capacities of control concrete specimen without ECC layer (BA-0, BA-50, BA-100 and BA-150) in each group. M_{qc} and d_q are the moment and corresponding deflection under quasi-permanent combinations of control concrete specimen, respectively.

As observed from Table 7, the bending capacities of ECC-concrete composite specimens (group BB and BC) and ECC specimens (group BD) are greater than that of concrete specimens (group BA). Compared with the control specimen BA-0, the bending capacities improvement of BB-0, BC-0 and BD-0 are 4%, 28% and 12%, respectively. Specimens subjected to 50, 100 and 150 cycles show the same trend. For unfrozen specimens, the deflections of specimen BB-0, BC-0 and BD-0 under the

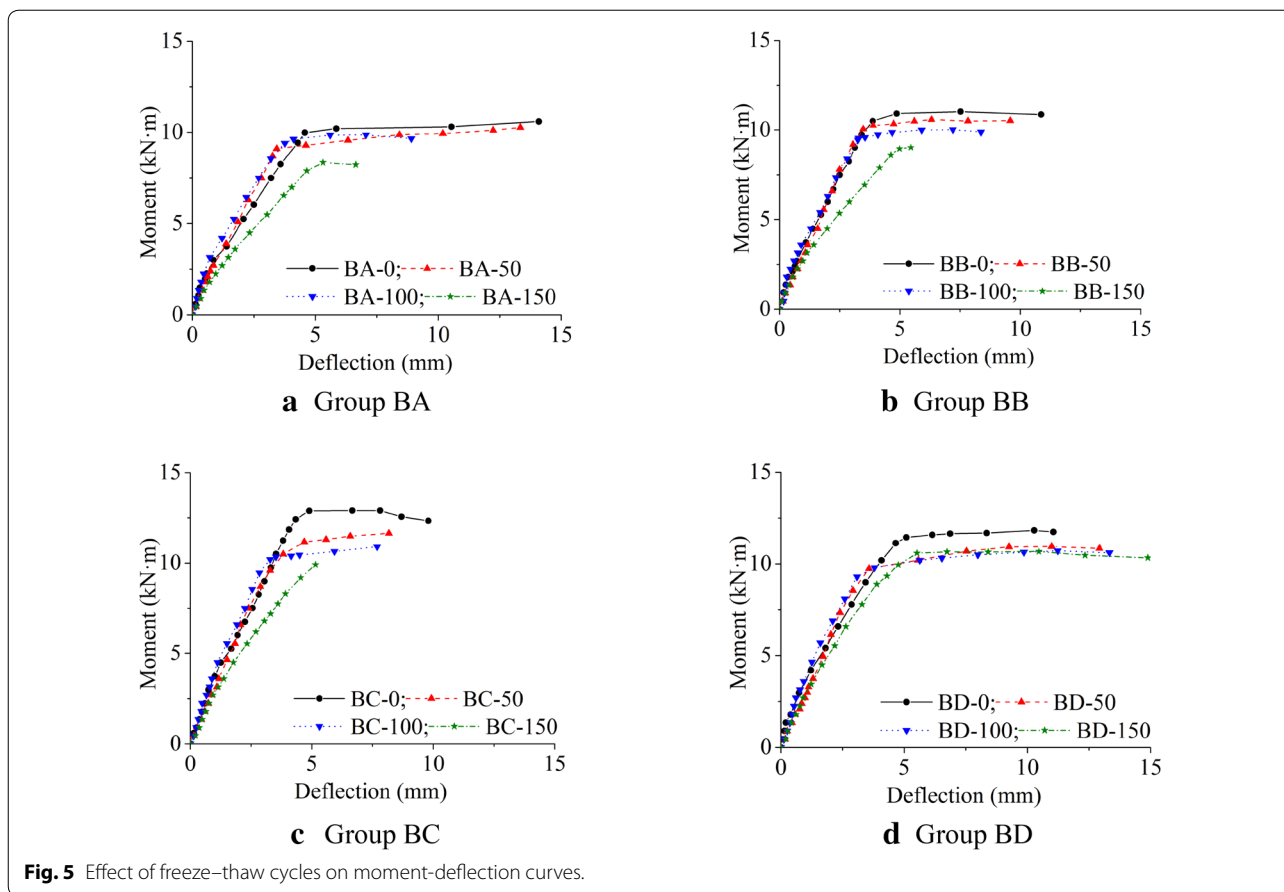


Fig. 5 Effect of freeze–thaw cycles on moment-deflection curves.

Table 6 Comparison of bending capacity and deflection—taking unfrozen specimen as control specimen.

No.	M_u (kN m)	$M_{u,i}/M_{u,0}$	$M_{q,0}$ (kN m)	d_q (mm)	$d_{q,i}/d_{q,0}$
BA-0	10.60	1.00	6.78	2.85	1.00
BA-50	10.27	0.97	2.49	0.87	
BA-100	9.87	0.93	2.35	0.82	
BA-150	8.35	0.79	3.89	1.36	
BB-0	11.02	1.00	7.05	2.35	1.00
BB-50	10.58	0.96	2.30	0.98	
BB-100	10.01	0.91	2.24	0.95	
BB-150	9.02	0.82	3.60	1.53	
BC-0	13.60	1.00	8.70	2.96	1.00
BC-50	11.64	0.86	2.89	0.97	
BC-100	10.92	0.80	2.60	0.88	
BC-150	9.91	0.73	4.20	1.42	
BD-0	11.82	1.00	7.56	2.76	1.00
BD-50	10.95	0.93	2.49	0.90	
BD-100	10.72	0.91	2.27	0.82	
BD-150	10.60	0.90	3.16	1.14	

quasi-permanent moment combinations are 79%, 81% and 85% of that of the control concrete specimen BA-0, respectively. Similar trends to specimens subjected to 50, 100 and 150 cycles, illustrating the bending capacity and flexural stiffness are improved when the tension zone was replaced by ECC layer.

3.3 Maximum Crack Width

Figure 6 presents the tested maximum crack widths at the same height of steel reinforcement for various load. $\omega_{max,lim}$ is the crack width limit value (Liu et al. 2008) and τ_l is the crack widths amplification coefficient under long-term load action (China Academy of Building Research 2010) of reinforced concrete specimen, $\omega_{max,lim}/\tau_l$ is the limit value under testing load. Table 9 presents the crack width of specimens under the quasi-permanent moment combinations of tested control concrete specimens. M_{qc} and ω_q are the moment under quasi-permanent combinations of specimen BA-0 and the corresponding crack width, respectively. The average crack spacing l_{cr} and number of cracks n_{cr} are also presented in Fig. 7.

Table 7 Comparison of bending capacity and deflection - taking concrete specimen as control specimen.

No.	M_u (Kn m)	$M_{u,i}/M_{u,c}$	$M_{q,c}$ (kN m)	d_q (mm)	$d_{q,i}/f_{q,c}$	NO.	M_u (kN m)	$M_{u,i}/M_{u,c}$	$M_{q,c}$ (kN m)	d_q (mm)	$d_{q,i}/f_{q,c}$
BA-0	10.60	1.00	6.78	2.85	1.00	BA-50	10.27	1.00	6.57	2.39	1.00
BB-0	11.02	1.04		2.26	0.79	BB-50	10.95	1.07		2.17	0.91
BC-0	13.60	1.28		2.30	0.81	BC-50	11.64	1.13		2.06	0.86
BD-0	11.82	1.12		2.41	0.85	BD-50	10.81	1.05		2.16	0.90
BA-100	9.87	1.00	6.32	2.14	1.00	BA-150	8.35	1.00	5.34	2.93	1.00
BB-100	10.01	1.01		2.00	0.93	BB-150	9.02	1.08		2.49	0.85
BC-100	10.92	1.11		1.81	0.85	BC-150	9.91	1.19		2.23	0.76
BD-100	10.72	1.09		1.86	0.87	BD-150	10.60	1.27		2.09	0.71

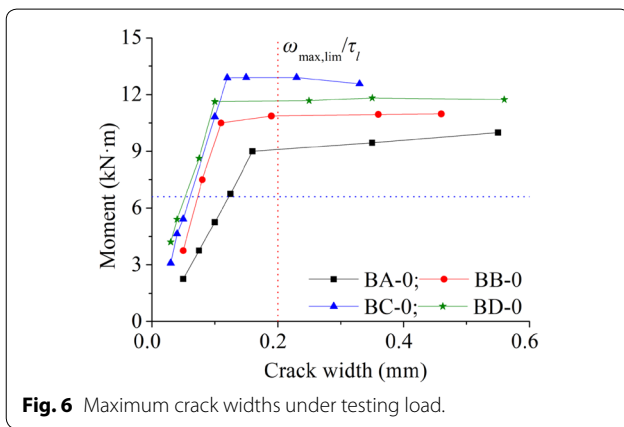


Fig. 6 Maximum crack widths under testing load.

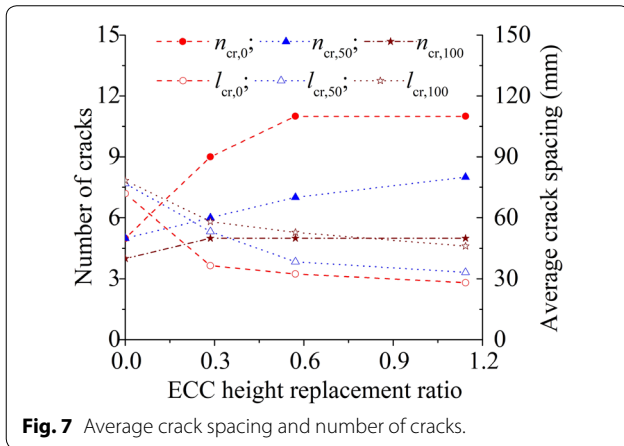


Fig. 7 Average crack spacing and number of cracks.

As can be seen from Figs. 6, 7 and Table 8, for unfrozen specimens, the crack width under quasi-permanent moment combinations of specimen BB-0, BC-0 and BD-0 are 59%, 50% and 44% of that of the control concrete specimen BA-0, respectively, indicating that crack widths decrease as the ECC height replacement ratios increase. It is also noted that the crack widths under quasi-permanent moment combinations all meet the requirement of service state, less than 0.2 mm. The average crack spacing

Table 8 Comparison of bending capacities and deflection—taking concrete specimen as control specimen.

No.	M_u (kN m)	$M_{u,i}/M_{u,c}$	$M_{q,c}$ (kN m)	ω_q (mm)	$\omega_{q,i}/\omega_{q,c}$
BA-0	10.60	1.00	6.78	0.13	1.00
BB-0	11.02	1.04		0.07	0.59
BC-0	13.60	1.28		0.06	0.50
BD-0	11.82	1.12		0.05	0.44

decreases while number of cracks increases as the ECC height replacement ratios increase, illustrating that the application of ECC can control the cracks distributed along the specimens tensile zone effectively.

3.4 Failure Modes

Typical under-reinforced flexural failure occurred for all specimens where steel reinforcement yielded, followed by crushing of concrete/ECC in the compressive zone (concrete for reinforced concrete specimens (group BA) and ECC-concrete composite specimens (group BB and BC), ECC for reinforced ECC specimens (group BD)). Fig 8 presents the failure modes of representative specimens. For unfrozen concrete specimens (for example specimen BA-0), after yielding of steel reinforcement, several visible cracks occurred near failure and, finally, the concrete compressive zone crushed. For concrete specimens subjected to freeze–thaw cycles (for example specimen BA-150), large volume of mortars dropped out and gravels exposed, several visible cracks occurred in the tensile zone. After yielding of steel reinforcement, a major crack occurred near failure and, finally, the concrete compressive zone crushed. For unfrozen composite specimens (for example specimen BC-0), multi-cracks occurred in the tensile zone, with the increase of loading, many new cracks developed and, then the steel reinforcement yield, finally, the concrete compressive zone crushed. For composite specimens subjected to freeze–thaw cycles (for example specimen BC-50, BC-100 and BC-150),

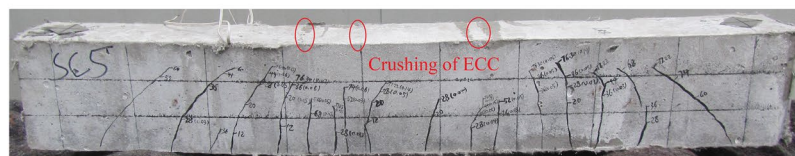
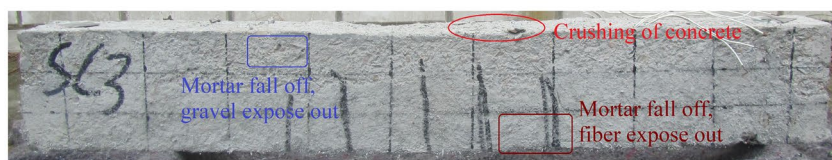
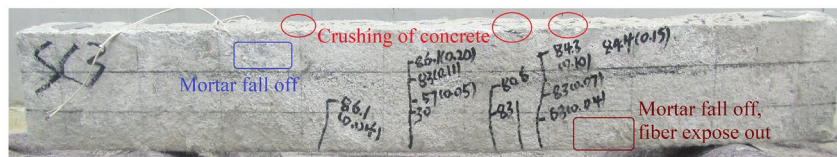
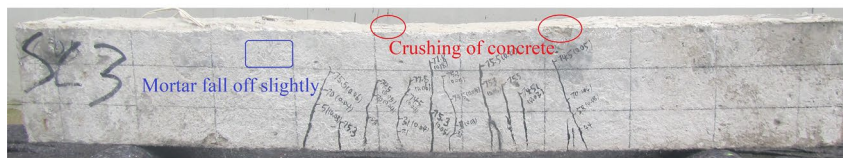
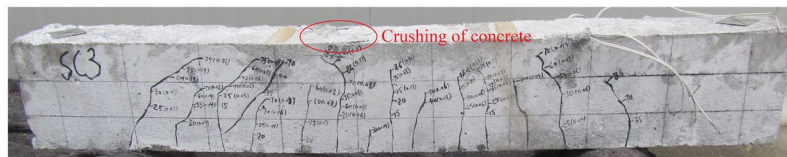
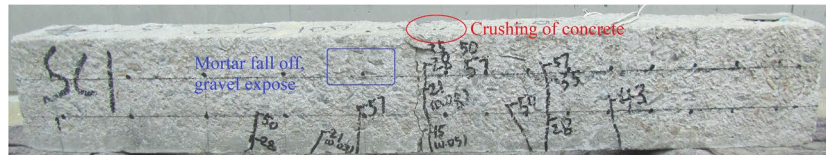
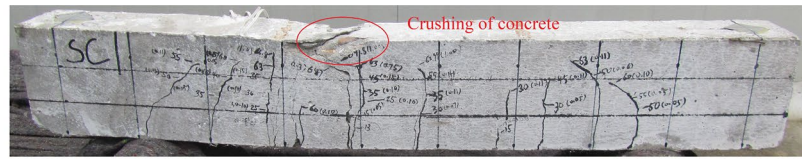


Fig. 8 Failure modes of selected test specimens.

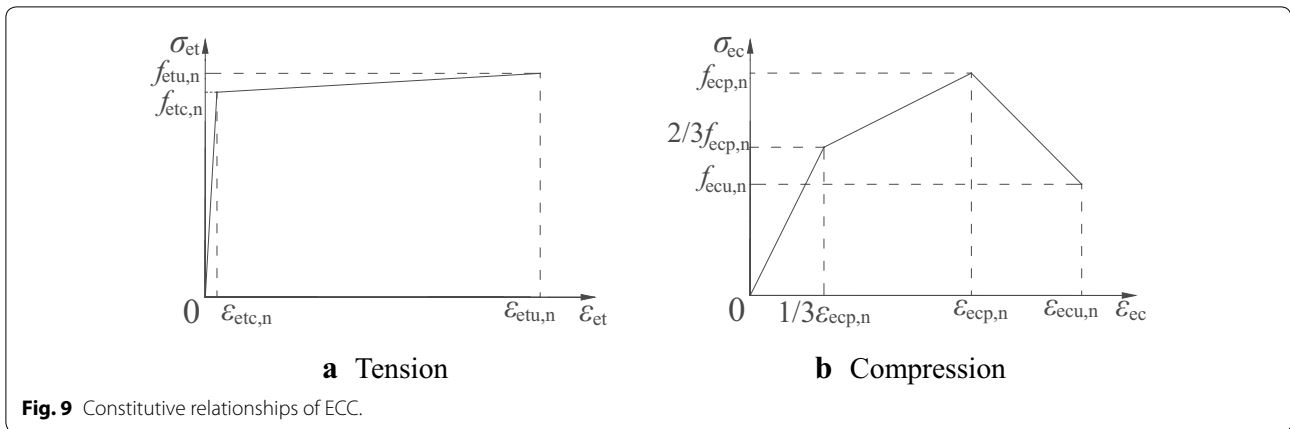


Fig. 9 Constitutive relationships of ECC.

with increasing the freeze–thaw cycles, mortar dropped out, and the bottom ECC layer exposed more fiber while the upper concrete layer exposed more sand and gravel. After yielding of steel reinforcement, several visible cracks occurred near failure and, finally, the concrete compressive zone crushed. For ECC specimens, the initial characteristics were similar to ECC-concrete composite specimens. After yielding of steel reinforcement, the outermost layer of ECC specimens reached its ultimate strain and then crushed, but the fibers distributed in cementitious materials can hold the crushed ECC blocks in contact.

4 Theoretical Analysis

4.1 Basic Assumption

The following assumptions have been considered in developing the predictions of flexural performance of steel reinforced ECC-concrete composite beams subjected to freeze–thaw cycles:

- The three materials used in beams tested, namely, concrete, ECC and steel bars, have perfect bond with each other. This assumption is validated in the current experimental investigation and other previous studies (Ge et al. 2018; ACI Committee 224 2001).
- Beam cross-section perpendicular to the neutral axis before loading remains plane after loading (Ge et al. 2018) as shown in Fig. 3.
- The concrete tensile force at failure is neglected. Although concrete close to the neutral axis is not cracked, the tensile force of uncrack concrete and its moment is small and also ignored.
- According to the experimental observation of load–deformation relationship, there exist three obvious stages (Ge et al. 2018), uncracked stage (elastic stage), service stage and failure stage.
- The following simplified constitutive relationships are used.

The constitutive model of steel bars (China Academy of Building Research 2010) simplified to a bilinear curve is expressed as Eq. 1. ϵ_s and σ_s are the steel reinforcement’s strain and stress, respectively, E_s and f_{sy} are the modulus of elasticity and the yield strength, respectively, ϵ_{sy} and ϵ_{su} are the yield and ultimate tensile strain.

$$\sigma_s = \begin{cases} E_s \epsilon_s, & 0 \leq \epsilon_s \leq \epsilon_{sy} \\ f_y, & \epsilon_{sy} < \epsilon_s \leq \epsilon_{su} \end{cases} \quad (1)$$

The tensile constitutive model of ECC (Li et al. 2001) simplified to a bilinear curve is shown in Fig. 9a and presented by Eq. 2 as below. ϵ_{et} and σ_{et} are the ECC material’s tensile strain and stress, respectively. $\epsilon_{etc,n}$ and $\epsilon_{etu,n}$ are the ECC material’s cracking and ultimate strain subjected to n freeze–thaw cycles, respectively. $f_{etc,n}$ and $f_{etu,n}$ are the cracking and ultimate stresses subjected to n freeze–thaw cycles, respectively.

$$\sigma_{et} = \begin{cases} \frac{f_{etc,n}}{\epsilon_{etc,n}} \epsilon_{et}, & 0 < \epsilon_{et} \leq \epsilon_{etc,n} \\ f_{etc,n} + \frac{f_{etu,n} - f_{etc,n}}{\epsilon_{etu,n} - \epsilon_{etc,n}} (\epsilon_{et} - \epsilon_{etc,n}), & \epsilon_{etc,n} < \epsilon_{et} \leq \epsilon_{etu,n} \end{cases} \quad (2)$$

The mechanical properties of ECC subjected to n freeze–thaw cycles established by regression analysis of the tested data are expressed as follows.

$$f_{etc,n} = f_{etc,0}(-0.00119n + 0.98762) \quad (3)$$

$$f_{etu,n} = f_{etu,0}(-0.00116n + 1.00747) \quad (4)$$

$$\epsilon_{etc,n} = \epsilon_{etc,0}(0.0025n + 1.0) \quad (5)$$

$$\epsilon_{etu,n} = \epsilon_{etu,0}(0.00152n + 1.00112). \quad (6)$$

The compressive constitutive model of ECC (Yuan et al. 2013) simplified to a trilinear curve is shown in Fig. 9b and expressed by Eq. 7. ε_{ec} and σ_{ec} are the ECC material's compressive strain and stress, respectively; $f_{ecp,n}$ and $f_{ecu,n}$ are the maximum (peak point) and ultimate (after peak point) stress, respectively; $\varepsilon_{ecp,n}$ and $\varepsilon_{ecu,n}$ are the strain corresponding to maximum and ultimate compressive stress, respectively, subjected to n freeze–thaw cycles.

$$\sigma_{ec} = \begin{cases} 2 \frac{f_{ecp,n}}{\varepsilon_{ecp,n}} \varepsilon_{ec}, & 0 \leq \varepsilon_{ec} \leq \varepsilon_{ecp,n}/3 \\ \frac{f_{ecp,n}}{2} + \frac{f_{ecu,n}}{2\varepsilon_{ecu,n}} \varepsilon_{ec}, & \varepsilon_{ecp,n}/3 < \varepsilon_{ec} \leq \varepsilon_{ecp,n} \\ 2f_{ecu,n} - \frac{f_{ecp,n}}{\varepsilon_{ecp,n}} \varepsilon_{ec}, & \varepsilon_{ecp,n} < \varepsilon_{ec} \leq \varepsilon_{ecu,n} \end{cases} \quad (7)$$

The compressive values of ECC subjected to n freeze–thaw cycles as required by Eq. (7) established by regression analysis of the tested data are expressed as follows.

$$f_{ecp,n} = f_{ecp,0}(-0.00120n + 1.00666) \quad (8)$$

$$f_{ecu,n} = f_{ecu,0}(-0.00120n + 1.00662) \quad (9)$$

$$\varepsilon_{ecp,n} = \varepsilon_{ecp,0}(0.00167n + 1.0) \quad (10)$$

$$\varepsilon_{ecu,n} = \varepsilon_{ecu,0}(0.00167n + 1.0). \quad (11)$$

The compressive constitutive model of concrete (Hognestad 1951; Wang 2017) simplified to a parabolic curve is shown in Fig. 10a and expressed by Eq. 12. $f_{c,n}$ and $f_{cu,n}$ are the maximum (peak point) and ultimate stress (after peak point), respectively; $\varepsilon_{co,n}$ and $\varepsilon_{cu,n}$ are the strain corresponding to maximum and ultimate stress, respectively, subjected to n freeze–thaw cycles. ε_c and σ_c are the concrete compressive strain and corresponding stress.

$$\sigma_c = \begin{cases} f_{c,n} \left[2\varepsilon_c/\varepsilon_{co,n} - (\varepsilon_c/\varepsilon_{co,n})^2 \right], & 0 \leq \varepsilon_c \leq \varepsilon_{co,n} \\ f_{c,n} \left[1 - 0.15 \frac{\varepsilon_c - \varepsilon_{co,n}}{\varepsilon_{cu,n} - \varepsilon_{co,n}} \right], & \varepsilon_{co,n} < \varepsilon_c \leq \varepsilon_{cu,n} \end{cases} \quad (12)$$

The predicted compressive performances of concrete subjected to n freeze–thaw cycles established by regression analysis of experimental data are expressed as follows.

$$f_{c,n} = f_{c,0}(-0.00284n + 0.96128) \quad (13)$$

$$f_{cu,n} = f_{cu,0}(-0.00284n + 0.96125) \quad (14)$$

$$\varepsilon_{co,n} = \varepsilon_{co,0}(0.01370n + 0.95890) \quad (15)$$

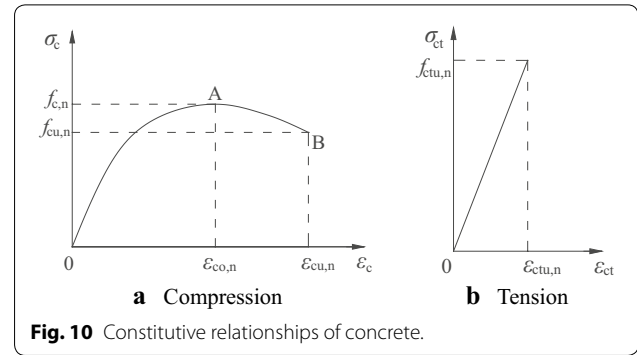


Fig. 10 Constitutive relationships of concrete.

$$\varepsilon_{cu,n} = \varepsilon_{cu,0}(0.01054n + 0.98382). \quad (16)$$

The tensile constitutive model of concrete (China Academy of Building Research 2010; Cao et al. 2012) is simplified to a linear curve as shown in Fig. 10b and presented by Eq. 17 as below. $\varepsilon_{ctu,n}$ and $f_{ctu,n}$ are the concrete ultimate tensile strain and stress subjected to n freeze–thaw cycles, respectively. ε_{ct} and σ_{ct} are the strain and corresponding stress in tensile concrete, respectively.

$$\sigma_{ct} = \frac{f_{ctu,n}}{\varepsilon_{ctu,n}} \varepsilon_{ct}, \quad 0 \leq \varepsilon_{ct} \leq \varepsilon_{ctu,n}. \quad (17)$$

The predicted tensile performances of concrete subjected to n freeze–thaw cycles established by regression analysis of experimental data are expressed as follows.

$$f_{ctu,n} = f_{ctu,0}(-0.0040n + 1.0114) \quad (18)$$

$$\varepsilon_{ctu,n} = \varepsilon_{ctu,0}(-0.0039n + 1.0139). \quad (19)$$

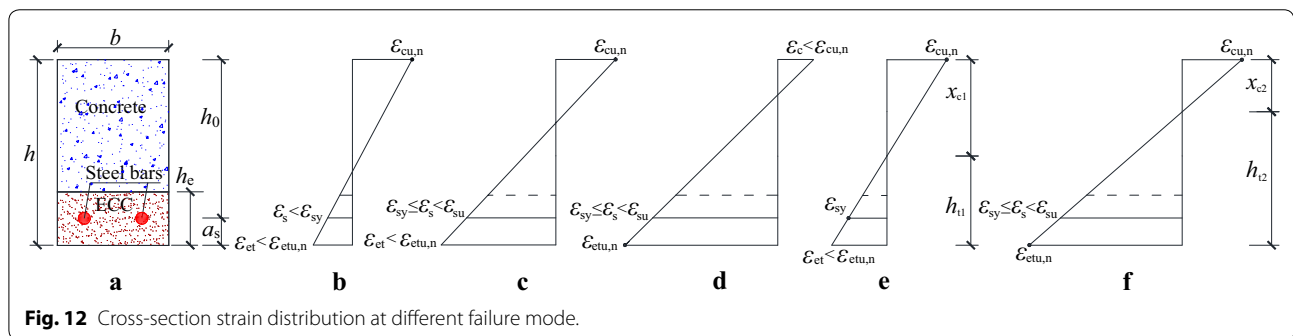
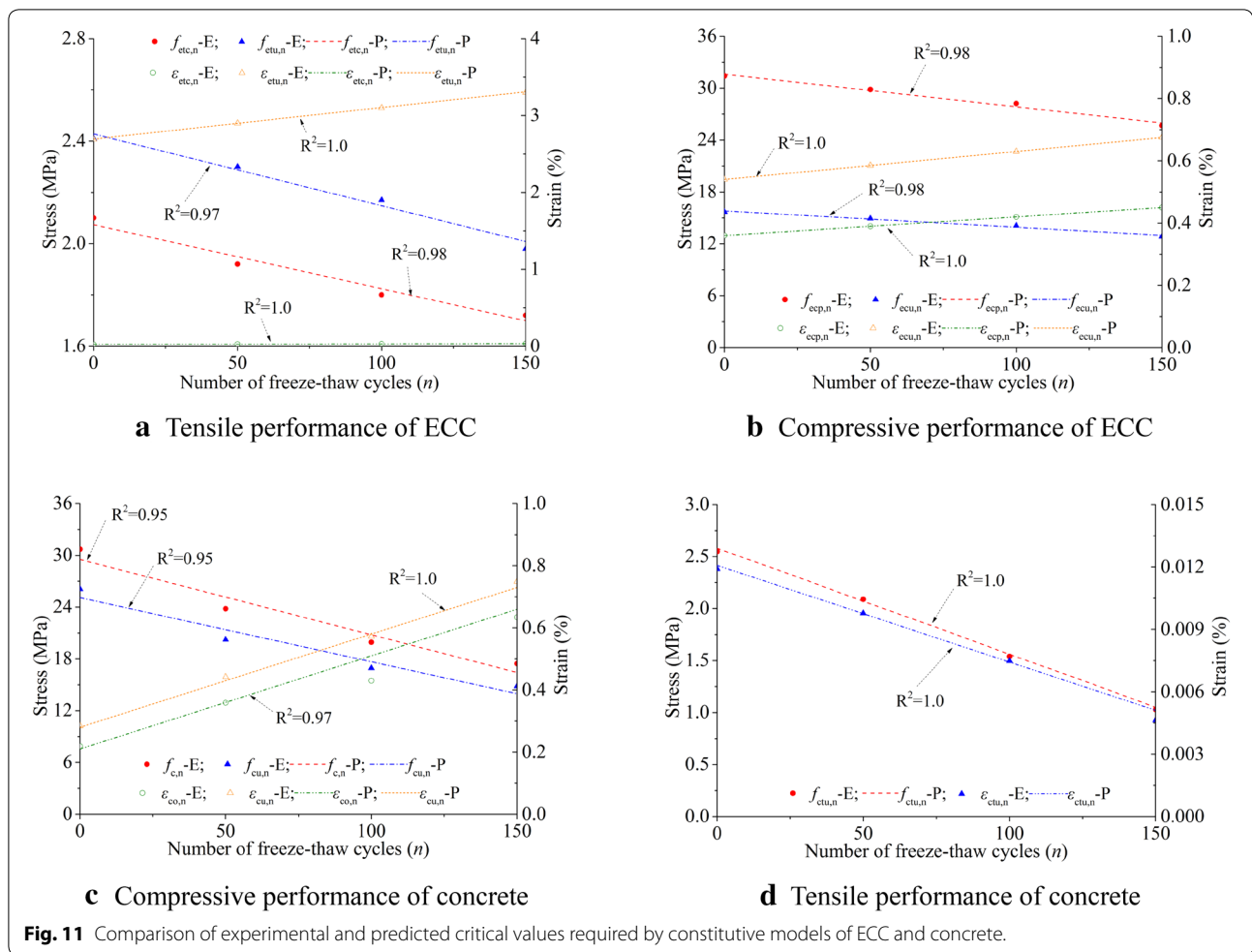
Comparisons of experimental and predicted mechanical performances of ECC and concrete subjected to n freeze–thaw cycles are shown in Fig. 11, where R^2 is the coefficient of determination.

As observed from Fig. 11, the coefficients of determination are, all, greater than 0.95, showing good agreement between the predicted critical values and experimental test results.

4.2 Analysis of Cross-Section

4.2.1 Failure Modes

Based on the materials' simplified constitutive (stress–strain curves) models, two failure modes occurred for ECC-concrete composite specimens, namely tensile or compressive failure. In Fig. 12, failure modes can be identified as following and their corresponding strain distribution are given. ① Compressive failure before steel reinforcement yielding (over-reinforced case): $\varepsilon_c = \varepsilon_{cu,n}$,



$\epsilon_s < \epsilon_{sy}$, $\epsilon_{et} < \epsilon_{etu,n}$, as shown in Fig. 12b. ② Compressive failure 2 after yielding of steel: $\epsilon_c = \epsilon_{cu,n}$, $\epsilon_{sy} \leq \epsilon_s < \epsilon_{su}$, $\epsilon_{et} < \epsilon_{etu,n}$, as shown in Fig. 12c. ③ Tensile failure: $\epsilon_c < \epsilon_{cu,n}$, $\epsilon_s < \epsilon_{su}$, $\epsilon_{et} = \epsilon_{etu,n}$, as shown in Fig. 12d. Where ϵ_{et} is the ECC bottom tensile strain, ϵ_s is the steel bars tensile strain, ϵ_c and ϵ_{ct} are the concrete maximum compressive and tensile strain, respectively. h and b are the height and

width of cross-section, h_e is the height of ECC, a_s is the vertical distance between the cross-section bottom edge and the centroid of steel bars, h_0 is the effective height of cross-section, $h_0 = h - a_s$, h_t is the tensile height (neutral axis depth) of cross-section, x_c is the compressive height (above the neutral axis) of cross-section.

4.2.2 Failure modes discrimination

When $\varepsilon_c = \varepsilon_{cu,n}$ and $\varepsilon_s = \varepsilon_{sy}$ simultaneously take place, as shown in Fig. 12e, balanced failure 1 occurs. If $\varepsilon_c = \varepsilon_{cu,n}$ and $\varepsilon_{et} = \varepsilon_{etu,n}$ simultaneously take place, as shown in Fig. 12f, balanced failure 2 occurs.

According to triangle similarity, the relative compressive height ξ , which is defined as the cross-section compressive height x_c to the effective height h_0 , $\xi = x_c/h_0$, for two balanced failure stage, can be expressed as follows. For balanced failure 1:

$$\xi_{cb1} = \frac{x_{c1}}{h_0} = \frac{\varepsilon_{cu,n}}{\varepsilon_{cu,n} + \varepsilon_{sy}} \quad (20)$$

For balanced failure 2:

$$\xi_{cb2} = \frac{x_{c2}}{h_0} = \frac{x_{c2}}{h} \cdot \frac{h}{h_0} = \frac{\varepsilon_{cu,n}}{\varepsilon_{cu,n} + \varepsilon_{etu,n}} \cdot \frac{h}{h_0} \quad (21)$$

If $\xi > \xi_{cb1}$, failure mode ① occurs; if $\xi_{cb2} \leq \xi \leq \xi_{cb1}$, failure mode ② occurs; and if $\xi < \xi_{cb2}$, failure mode ③ occurs.

The following equation can be obtained on the base of cross-section force equilibrium.

$$\int_0^{x_c} \sigma_c b dx = \sigma_s A_s + \int_0^{h_e} \sigma_{et} b dx \quad (22)$$

where σ_c and σ_{et} are the concrete compressive stress and ECC tensile stress, respectively, A_s and σ_s are the steel bars cross-sectional area and tensile stress, respectively.

In order to simplify the calculation formula, considering $\sigma_{et} = f_{etc,n}$, Eq. (22) can be transformed into following. For balanced failure 1, $x_c = \varepsilon_{cu,n} h_0 / (\varepsilon_{cu,n} + \varepsilon_{sy})$.

$$f_{c,n} b h_0 \frac{\varepsilon_{cu,n} - \varepsilon_{co,n}/3}{\varepsilon_{cu,n} + \varepsilon_{sy}} = f_{sy} A_s + f_{etc,n} b h_e \quad (23)$$

Equation (23) can be transformed into the expression of reinforcement ratio, as below.

$$\rho_{s,b1} = \frac{f_{c,n}}{f_{sy}} \cdot \frac{\varepsilon_{cu,n} - \varepsilon_{co,n}/3}{\varepsilon_{cu,n} + \varepsilon_{sy}} - r_h \frac{f_{etc,n}}{f_{sy}} \quad (24)$$

For balanced failure 2, $x_c = \varepsilon_{cu,n} h / (\varepsilon_{cu,n} + \varepsilon_{etu,n})$, $\varepsilon_s = (\varepsilon_{etu,n} h_0 - \varepsilon_{cu,n} a_s) / h$.

$$f_{c,n} b h \frac{\varepsilon_{cu,n} - \varepsilon_{co,n}/3}{\varepsilon_{cu,n} + \varepsilon_{etu,n}} = f_{sy} A_s + f_{etc,n} b h_e \quad (25)$$

Equation (25) can be transformed into the expression of reinforcement ratio, as below.

$$\rho_{s,b2} = \frac{f_{c,n}}{f_{sy}} \frac{\varepsilon_{cu,n} - \varepsilon_{co,n}/3}{\varepsilon_{cu,n} + \varepsilon_{etu,n}} \frac{h}{h_0} - r_h \frac{f_{etc,n}}{f_{sy}} \quad (26)$$

$\rho_{s,b1}$ and $\rho_{s,b2}$ are defined as the maximum and minimum balanced reinforcement ratio, respectively. So, if $\rho_s > \rho_{s,b1}$,

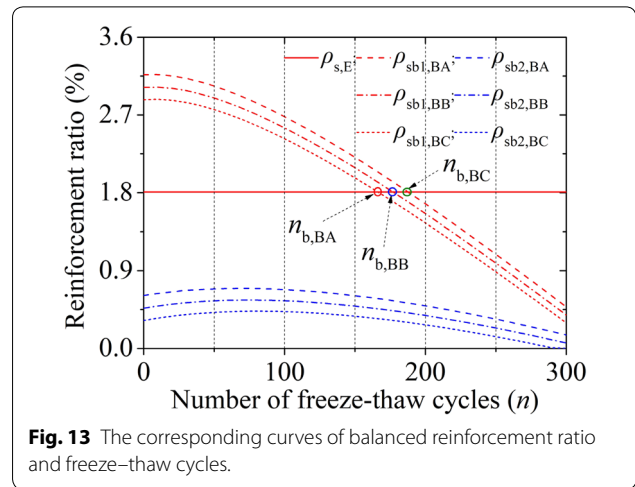


Fig. 13 The corresponding curves of balanced reinforcement ratio and freeze-thaw cycles.

failure mode ① occurs; if $\rho_{s,b2} \leq \rho_s \leq \rho_{s,b1}$, failure mode ② occurs; if $\rho_s < \rho_{s,b2}$, failure mode ③ occurs.

4.2.3 Experimental verifications

The maximum and minimum balanced reinforcement ratio for ECC-concrete specimens subject to freeze-thaw cycles can be calculated by formulas (24) and (26). The balanced reinforcement ratio formulas for composite specimens can be also applied to concrete specimens by just substituting $f_{etc,n} = 0$. Figure 13 presents the corresponding curves of balanced reinforcement ratio against freeze-thaw cycles.

As observed from Fig. 13, with increasing the cycles of freeze-thaw, the minimum balanced reinforcement ratio $\rho_{s,b2}$, initially slightly increases, and, then, decreases, while the maximum balanced reinforcement ratio $\rho_{s,b1}$ gradually decreases. For this experimental investigation, the actual reinforcement ratio $\rho_s (= 1.8\%)$ is always greater than $\rho_{s,b2}$. However, $\rho_{s,b1}$ is initially greater than ρ_s (appropriate tensile failure occurs), but smaller than ρ_s (over-reinforced failure occurs) after certain cycles of freeze-thaw.

Comparisons of tested and predicted failure modes are presented in Table 9. CFM and EFM indicate calculated failure mode and experimental failure mode, respectively. SY, SNY and CC indicate steel yielded, steel not yielded and concrete crushed, respectively.

As observed from Table 9, the predicted failure modes show good agreement with that observed in the experiments.

4.3 Simplified Formula for Bending Capacity

In this section of the paper, simplified formulas for bending capacities of ECC-concrete composite and ECC specimens are developed as summarized in Table 10,

Table 9 Comparisons of experimental and predicted failure modes

No.	<i>n</i>	$\rho_s/\%$	$\rho_{s,b1}/\%$	$\rho_{s,b2}/\%$	$\rho_{s,b2} \leq \rho_s \leq \rho_{s,b1}$	CFM- ρ_s	EFM
BA	0	1.81	3.17	0.61	Yes	②	SY, CC
	50	1.81	3.03	0.69	Yes	②	SY, CC
	100	1.81	2.68	0.68	Yes	②	SY, CC
	150	1.81	2.21	0.61	Yes	②	SY, CC
BB	0	1.81	3.02	0.47	Yes	②	SY, CC
	50	1.81	2.90	0.55	Yes	②	SY, CC
	100	1.81	2.55	0.55	Yes	②	SY, CC
	150	1.81	2.09	0.49	Yes	②	SY, CC
BC	0	1.81	2.88	0.32	Yes	②	SY, CC
	50	1.81	2.76	0.42	Yes	②	SY, CC
	100	1.81	2.42	0.43	Yes	②	SY, CC
	150	1.81	1.97	0.37	Yes	②	SY, CC

Table 10 Simplified bending capacity formulas development for ECC-concrete composite and ECC specimens

	ECC-concrete composite specimen	ECC specimen
I-Strain and stress distribution		
II-Force equilibrium	$\alpha_{c,n} f_{c,n} b x = f_{s,y} A_s + f_{et,c,n} b h_e$	$\alpha_{e,n} f_{ecp,n} b x = f_{s,y} A_s + f_{et,c,n} b h_t$ (27)
III-Strain compatibility	$x_c (= x/\beta_{c,n}) + h_t = h$	$x_e (= x/\beta_{e,n}) + h_t = h$ (28)
IV-Equivalent resultant force	$\alpha_{c,n} f_{c,n} b \beta_{c,n} x_c = \int_0^{x_c} \sigma_c(y) b dy$	$\alpha_{e,n} f_{ecp,n} b \beta_{e,n} x_e = \int_0^{x_e} \sigma_{ec}(y) b dy$ (29)
V-Equivalent resultant moment	$\alpha_{c,n} f_{c,n} b \beta_{c,n} x_c (x_c - \beta_{c,n} x_c/2) = \int_0^{x_c} \sigma_c(y) b y dy$	$\alpha_{e,n} f_{ecp,n} b \beta_{e,n} x_e (x_e - \beta_{e,n} x_e/2) = \int_0^{x_e} \sigma_{ec}(y) b y dy$ (30)
VI-Neutral axis formula	$x = \frac{f_{s,y} A_s}{\alpha_{c,n} f_{c,n} b} + \frac{f_{et,c,n} h_e}{\alpha_{c,n} f_{c,n}}$	$x = \frac{f_{s,y} A_s/b + f_{et,c,n} h}{\alpha_{e,n} f_{ecp,n} + f_{et,c,n}/\beta_{e,n}}$ (31)
VII-Moment capacity formula	$M_u = f_{s,y} A_s (h_0 - x/2) + f_{et,c,n} b h_e (h - h_e/2 - x/2)$	$M_u = f_{s,y} A_s (h_0 - x/2) + f_{et,c,n} b h_t (h - h_t/2 - x/2)$ (32)

where the first row (I) presents the cross-section (a), strain distribution (b) as well as actual and simplified stress distributions (c) along the cross-section height of ECC-concrete composite specimen and ECC specimen, respectively, for failure mode ②.

Based on force equilibrium, Eq. (27) can be obtained, while Eq. (28) obtained according to the plane-section assumption. x_c and x_e are the height of concrete and ECC compressive stresses, respectively, x is the simplified height for compressive stress block ($x = \beta_{c,n} x_c$ for ECC-concrete composite specimen and $x = \beta_{e,n} x_e$ for ECC specimen), $\alpha_{c,n}$, $\alpha_{e,n}$, $\beta_{c,n}$ and $\beta_{e,n}$ are coefficients associated with the equivalent compressive stress distribution for concrete and ECC subjected to freeze–thaw cycles.

Then, based on the resultant force and moment equivalent principle, Eqs. (29) and (30) can be obtained. Substituting the concrete compressive properties into Eqs. (29) and (30), $\alpha_{c,n}/\alpha_{e,n}$ and $\beta_{c,n}/\beta_{e,n}$ can be calculated as presented in Table 11.

Rearranging Eq. (27) for x , Eq. (31) can be obtained. Then, taking moment about the resultant compressive force in concrete/ECC, the simplified formula for the bending capacity can be obtained as expressed in formula (32).

Table 12 presents comparisons of tested and predicted bending capacity, where $M_{u,e}$, $M_{u,c}$ are the experimental and predicted bending capacity, respectively.

As observed from Table 12, the average value and their variation coefficients of $M_{u,c}/M_{u,e}$ are 0.93 and 0.06,

Table 11 Values of simplified coefficients $\alpha_{c,n}$, $\beta_{c,n}$, $\alpha_{e,n}$ and $\beta_{e,n}$ for freeze–thaw cycles

<i>n</i>	Concrete		ECC	
	$\alpha_{c,n}$	$\beta_{c,n}$	$\alpha_{e,n}$	$\beta_{e,n}$
0	0.80	0.90	1.00	0.75
50	0.79	0.90	1.00	0.75
100	0.81	0.91	1.00	0.75
150	0.78	0.90	1.00	0.75

respectively, indicating the predicted bending capacity agrees well with tested results.

5 Parametric study

The influence of multi-parameters, for example the amount of steel reinforcement, height and strength of ECC, concrete strength and freeze–thaw cycles on the flexural performance of reinforced ECC-concrete composite beams are analyzed in this section. The cross-section width $b=100$ mm and height $h=150$ mm, respectively. The vertical distance of the centroid of steel reinforcement to the cross-section tensile edge $a_s=25$ mm, the cross-section effective height $h_0=125$ mm.

When one main parameter changes, other basic parameters of unfrozen tested specimens are maintained constant. Reinforcement ratio is 1.2%, steel yield strength is 400 N mm^{-2} , ECC height replacement ratio is 0.48. Concrete compressive strength and ultimate strain are 26.8 N mm^{-2} and 0.003522, respectively. ECC tensile cracking strength and strain are 5.0 N mm^{-2} and 0.00032, respectively. ECC ultimate tensile strength and strain are 5.0 N mm^{-2} and 0.03, respectively. The simplified constitutive relationships proposed in Sect. 4.1 are used to predict the mechanical properties of ECC and concrete subjected to freeze–thaw cycles.

The specimen is considered to be failed when tensile strains in reinforcement, ϵ_s , top concrete maximum

compressive strain, ϵ_c , or bottom ECC maximum tensile strains, ϵ_{et} , reaches their respective ultimate strain.

M_y and M_u represent yield moment and ultimate moment, respectively. ϕ_y , ϕ_u and ϕ_{ϕ} represent yield curvature, ultimate curvature and curvature ductility, $u_{\phi} = \phi_u / \phi_y$. E_e , E_p and r_E represent elastic energy dissipation (the area included in the elastic section of moment–curvature curve), plastic energy dissipation (the area included in the whole section of moment–curvature curve) and energy dissipation ratio, $r_E = E_p / E_e$.

5.1 Steel Reinforcement Ratio

Figure 14 represents the relationship curves of ultimate moment and curvature ductility against the steel reinforcement ratio. Five steel reinforcement ratios ρ_s , 0.4%, 0.8%, 1.2%, 1.6% and 2.4% are studied.

As observed from Fig. 14, with the increase of reinforcement ratio, the yield and ultimate moments gradually increase. The yield curvature increases, the ultimate curvature decreases and curvature ductility, thus, decreases gradually. The elastic energy dissipation increases, plastic energy dissipation decreases and energy dissipation ratio gradually decreases. After the reinforcement ratio exceed the maximum balanced reinforcement ratio $\rho_{sb1,n}$, the ultimate moment is equal to the yield moment and the plastic energy dissipation is also equal to the elastic energy dissipation.

Furthermore, with the increase of freeze–thaw cycles, the yield and the ultimate moments gradually decreases, the maximum balanced reinforcement ratio gradually decreases.

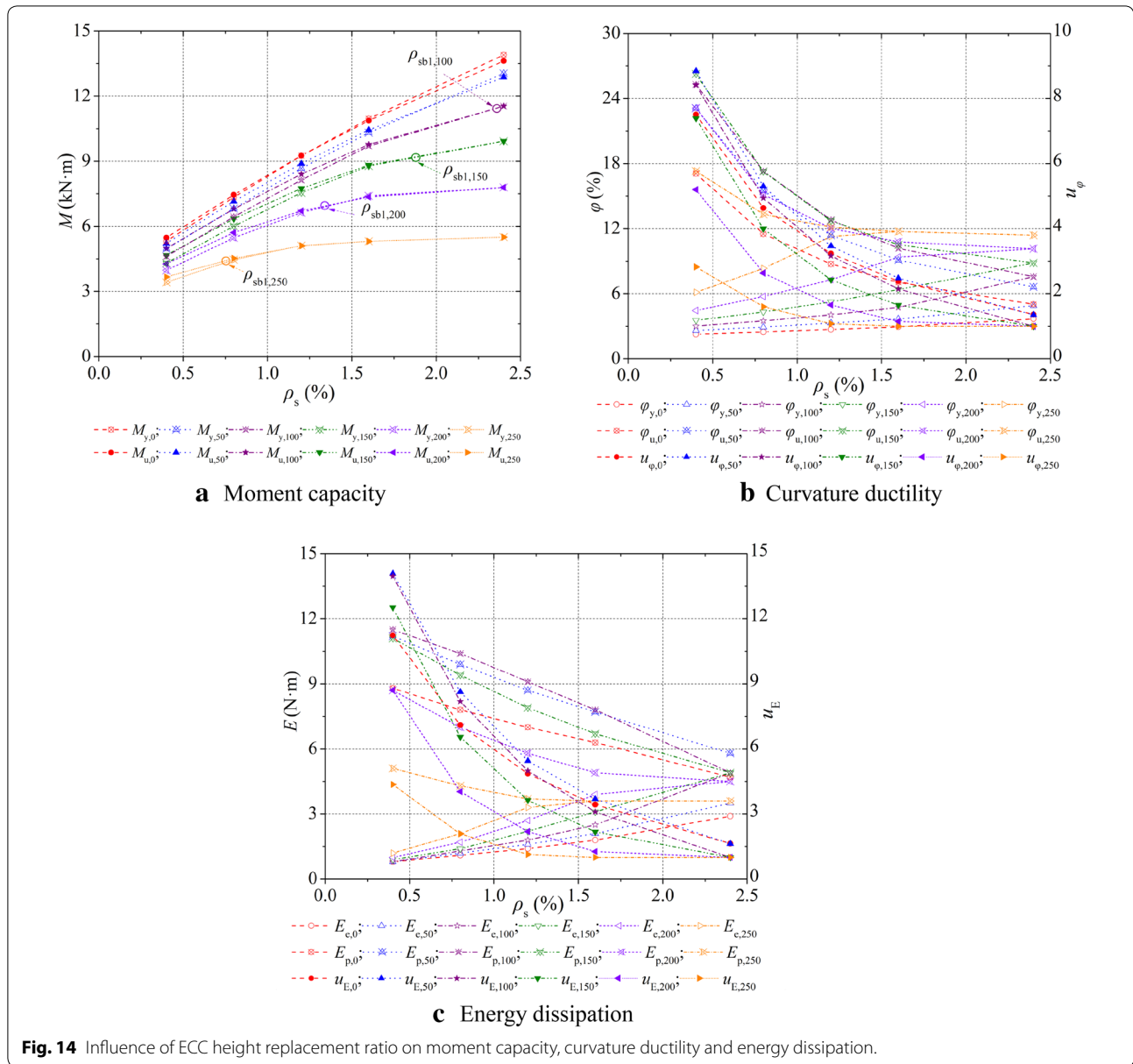
5.2 ECC Height Replacement Ratio

Figure 15 presents the relationship curves of ultimate moment and curvature ductility against the ECC height replacement ratio (0, 0.24, 0.48, 0.72, 0.96 and 1.20).

As observed from Fig. 15, with the increase of ECC replacement ratio, the yield and ultimate moment gradually increases. The yield curvature, first increase, and then decrease while the ultimate curvature, first decrease,

Table 12 Comparison of tested and predicted bending capacities

No.	<i>n</i>	$M_{u,e}$ (kN m)	$M_{u,c}$ (kN m)	$M_{u,c} / M_{u,e}$	No.	<i>n</i>	$M_{u,e}$ (kN m)	$M_{u,c}$ (kN m)	$M_{u,c} / M_{u,e}$
BA	0	10.60	9.73	0.92	BB	0	11.02	10.43	0.95
	50	10.27	9.39	0.91		50	10.58	9.99	0.94
	100	9.87	9.00	0.91		100	10.01	9.51	0.95
	150	8.35	8.21	0.98		150	9.02	8.57	0.95
BC	0	13.60	10.82	0.80	BD	0	11.82	11.34	0.96
	50	11.64	10.30	0.88		50	10.81	11.16	1.03
	100	10.92	9.74	0.89		100	11.51	10.97	0.95
	150	9.91	8.66	0.87		150	10.60	10.77	1.02



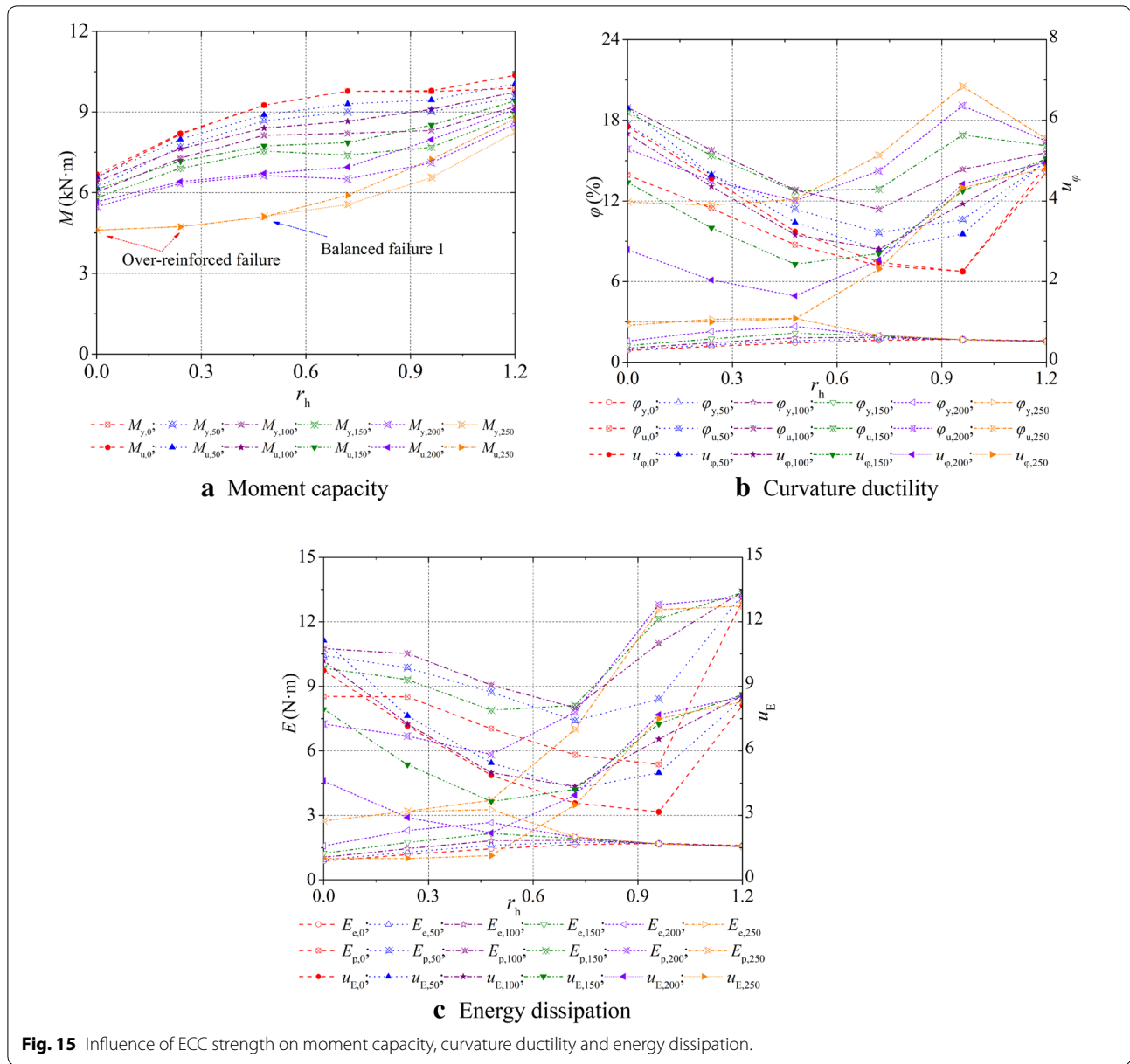
then increase, and then decrease; the curvature ductility, first decreases, and then increases, except for specimens exhibited over-reinforced failure. The elastic energy dissipation, first increases, and then decrease, the plastic energy dissipation, first decreases, and then increase, the energy dissipation ratio, first decreases, and then increase.

5.3 Strength of ECC

Figure 16 shows the relationship curves of ultimate moment and curvature ductility against the ECC strength. Five ECC grades, $f_{etc,A} = f_{etu,A} = 3.0 \text{ N mm}^{-2}$, $f_{ecp,A} = 30 \text{ N mm}^{-2}$, $f_{etc,B} = f_{etu,B} = 4.0 \text{ N mm}^{-2}$,

$f_{ecp,B} = 35 \text{ N mm}^{-2}$, $f_{etc,C} = f_{etu,C} = 5.0 \text{ N mm}^{-2}$, $f_{ecp,C} = 40 \text{ N mm}^{-2}$, $f_{etc,D} = f_{etu,D} = 6.0 \text{ N mm}^{-2}$, $f_{ecp,D} = 45 \text{ N mm}^{-2}$, $f_{etc,E} = f_{etu,E} = 7.0 \text{ N mm}^{-2}$, $f_{ecp,E} = 50 \text{ N mm}^{-2}$, $\epsilon_{etc} = 0.0003$, $\epsilon_{etu} = 0.03$, $\epsilon_{ecp} = 0.0036$ and $\epsilon_{ecu} = 0.0054$ are studied.

As observed from Fig. 16, with the improvement of ECC strength, the yield and ultimate moments gradually increase. The yield curvature gradually increases, the ultimate curvature gradually decreases, and hence the curvature ductility gradually decreases. The elastic energy dissipation increases, the plastic energy dissipation decreases, and hence the energy dissipation ratio gradually decreases.



5.4 Strength of Concrete

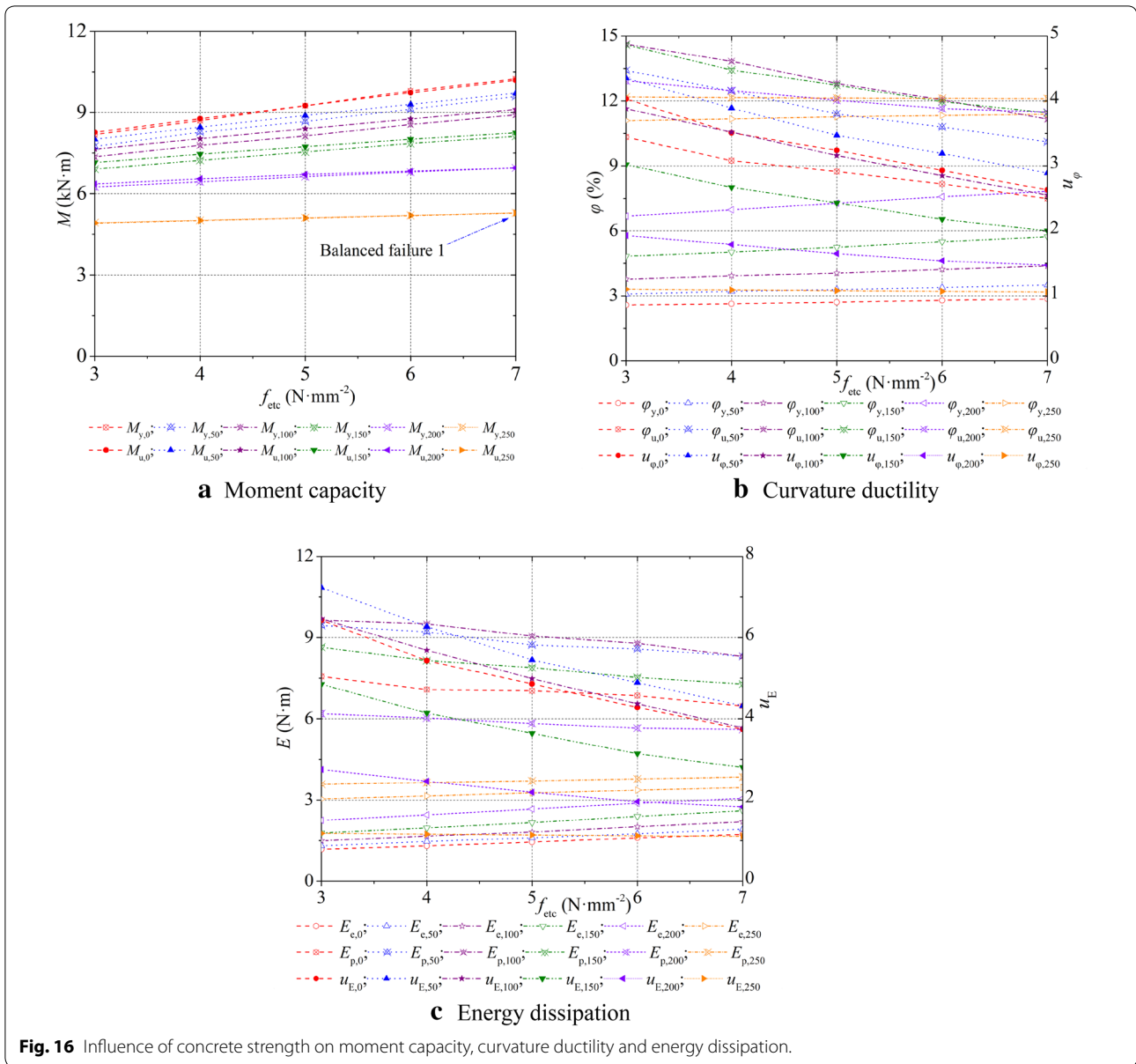
Figure 17 shows the relationship curves of ultimate moment and curvature ductility against the concrete strength. Five concrete compressive strength f_c , 20.1, 23.4, 26.8, 29.6 and 32.4 N mm^{-2} are studied.

As observed from Fig. 17, with the improvement of concrete strength, the yield and ultimate moment gradually increases. The yield curvature gradually decreases, the ultimate curvature gradually increases, and hence the curvature ductility gradually increases. The elastic energy dissipation decreases, the plastic energy dissipation increases, hence the energy dissipation ratio gradually increases.

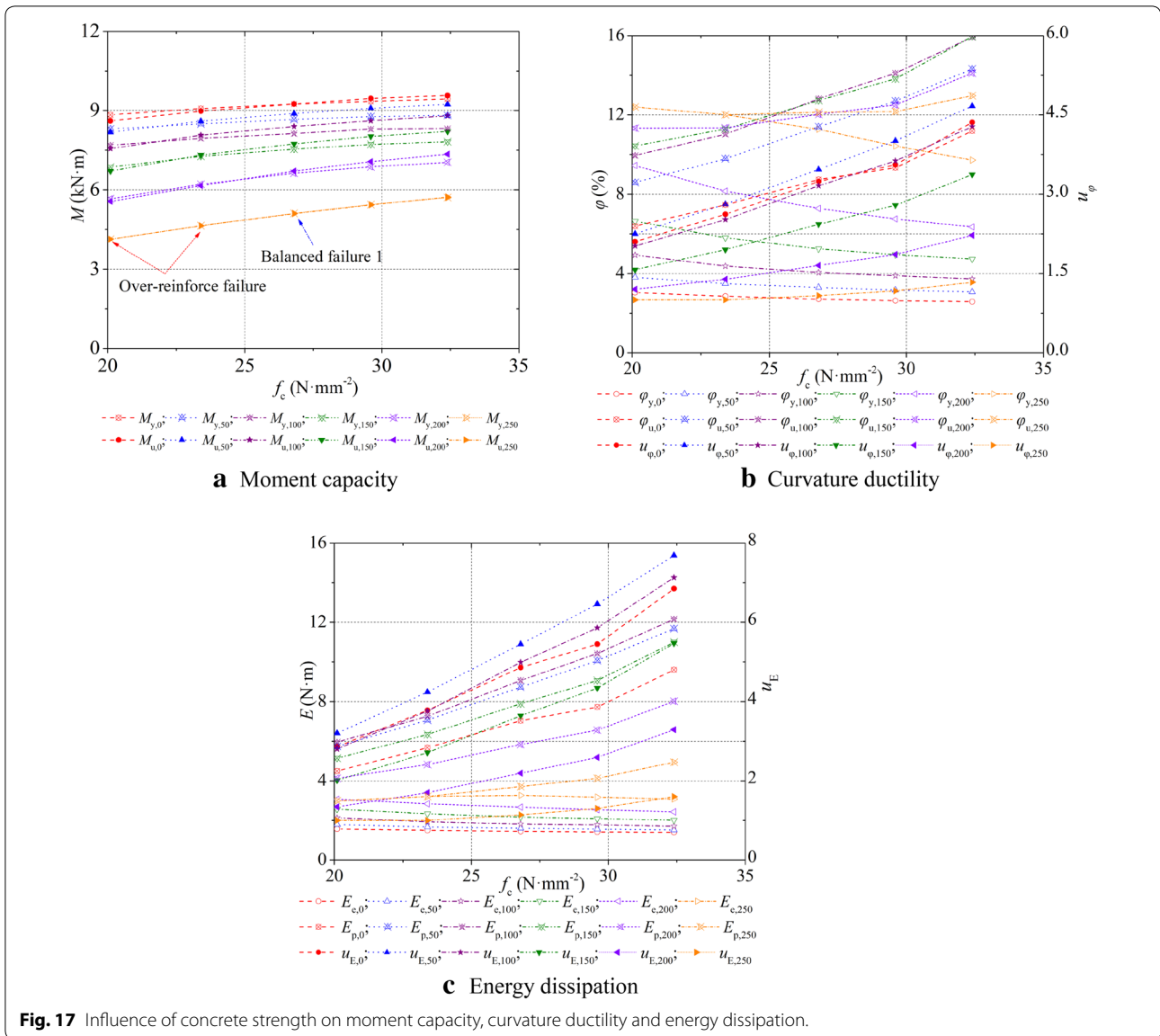
6 Conclusions

Experimental and theoretical investigations on the flexural performance of steel reinforced ECC-concrete composite beams subjected to freeze–thaw cycles are conducted. The following conclusions are drawn.

1. Three failure modes and two boundary failure states are proposed on the bases of plane-section assumption and materials constitutive models, and the discriminate formulas are also given. The predicted failure modes agree well with tested results.



2. The ultimate moments of ECC specimens and composite specimens are greater than those of traditional concrete beams. The deflection and crack width of ECC specimens and composite specimens are less than those of traditional concrete beams under the same load. The ECC layers placed in the tension zone can effectively improve specimens' deformation and cracks-resistance ability.
3. Based on the simplified materials' constitutive models and regression analysis of test results, the predicted mechanical performances of ECC and concrete subjected to freeze–thaw cycles are established.
4. With the increase of freeze–thaw cycles, the maximum balanced reinforcement ratio gradually decreases while the minimum balanced reinforcement ratio, initially slightly increases, and, then, decreases.
5. Simplified ultimate moment formulas are developed from simplified materials constitutive models and plane-section assumption. Experimental results show that the simplified formulas agree well with the test results, illustrating the validity of developed formulas.
6. Based on the parametric study conducted, it was shown that the yield and ultimate moments gradually increase with the increase of reinforcement ratio, ECC replacement height ratio as well as strengths of



concrete and ECC. On the other hand, as the ECC replacement ratio increases, the curvature ductility, first decreases, and then increases, except for over reinforced specimens.

Acknowledgements

The author would like to appreciate the financial support of the National Natural Science Foundation of China (51678514 and 51308490), China Postdoctoral Science Foundation (2018M642335), the Science and Technology Project of Jiangsu Construction System (2018ZD047), the Six Talent Peaks Project of Jiangsu Province (JZ-038, 2016) and Yangzhou University Top-level Talents Support Project. Special thanks for the editor, reviewers and their constructive comments and suggestions in improving the quality of this manuscript.

Authors' contributions

WG was a major contributor in the design of the study and collection, analysis, and interpretation of data and in writing the manuscript. AFA analyzed the

results of the experiment and improved the writing of the manuscript. WL operated the experiment and summed up the test data. DC improved the experimental program and interpreted the test data of the experiment. All authors read and approved the final manuscript.

Funding

The costs of construction of specimens and tests were paid by the following funding. Funder: the National Natural Science Foundation of China. Award number: 51678514 and 51308490. Funder: China Postdoctoral Science Foundation. Award number: 2018M642335. Funder: the Science and Technology Project of Jiangsu Construction System. Award number: 2018ZD047. Funder: the Six Talent Peaks Project of Jiangsu Province. Award number: JZ-038, 2016. Funder: Yangzhou University Top-level Talents Support Project.

Availability of data and materials

The datasets used and analysed during the current study are available from the corresponding author on reasonable request.

Competing interests

The authors declare that they have no competing interests.

Author details

¹ College of Civil Science and Engineering, Yangzhou University, Yangzhou 225127, China. ² School of Hydraulic, Energy and Power Engineering, Yangzhou University, Yangzhou 225127, China. ³ Faculty of Engineering and Informatics, University of Bradford, Bradford BD71DP, UK.

Received: 20 May 2019 Accepted: 11 December 2019

Published online: 17 February 2020

References

- ACI Committee 224. (2001). *Control of cracking in concrete structures ACI 224R-01* (p. 46). Farmington Hills: American Concrete Institute.
- Berry, M., Johnson, J., & McDevitt, K. (2017). Effect of cold temperatures on the behavior and ultimate capacity of GFRP-reinforced concrete beams. *Cold Regions Science and Technology*, 136, 9–16.
- Cao, D. F., Ge, W. J., Wang, B. Y., & Tu, Y. M. (2015). Study on the flexural behaviors of RC beams after freeze–thaw cycles. *Journal of Civil Engineering*, 131(1), 92–101.
- Cao, D. F., Fu, L. Z., & Yang, Z. W. (2012). Experimental study on tensile properties of concrete after freeze–thaw cycles. *Journal of Building Materials*, 15(1), 48–52.
- Cao, D. F., Qin, X. C., Meng, S. P., & Yongming, T. U. (2016). Evaluation of prestress losses in prestressed concrete specimens subjected to freeze–thaw cycles. *Structure and Infrastructure Engineering*, 12(2), 159–170.
- China Academy of Building Research. (2003). *Standard for test method of mechanical properties on ordinary concrete GB/T50081-2002*. Beijing: China Building Industry Press.
- China Academy of Building Research. (2010). *Code for design of concrete structures GB50010-2010*. Beijing: China Building Industry Press.
- China Renewable Energy Engineering Institute. (2006). *Test code for hydraulic concrete SL 352-2006*. Beijing: China Water & Power Press.
- Choi, W.-C., & Yun, H. D. (2015). Acoustic emission activity of CFRP-strengthened reinforced concrete beams after freeze–thaw cycling. *Cold Regions Science and Technology*, 110, 47–58.
- Diao, B., Sun, Y., & Ma, B. (2009). Experiment of persistent loading reinforced concrete beams under alternative actions of a mixed aggressive solution and freeze–thaw cycles. *Journal of Building Structures*, 52, 281–286.
- Ding, Y., Yu, K. Q., Yu, J. T., Xu, S. L. (2018). Structural behaviors of ultra-high performance engineered cementitious composites (UHP-ECC) beams subjected to bending-experimental study. *Construction and Building Materials*, 177, 102–115.
- Ge, W. J., Ashour, A. F., Ji, X., Cai, C., & Cao, D. F. (2018a). Flexural behavior of ECC-concrete composite beams reinforced with steel bars. *Construction and Building Materials*, 159, 175–188.
- Ge, W., Cai, C., Ji, X., Ashour, A. F., & Cao, D. (2018b). Experimental study of mechanical properties of PVA-ECC under freeze–thaw cycles. *Journal of Testing and Evaluation*, 46(6), 2330–2338.
- General Administration of Quality Supervision, Inspection and Quarantine of the People's Republic of China. (2002). *Metallic materials tensile testing at ambient temperature GB/T228-2002*. Beijing: Standards press of China.
- Hognestad, E. (1951). *Study of combined bending and axial load in reinforced concrete members*. Urbana: University of Illinois Engineering Experiment Station.
- Hung, C. C., & Su, Y. F. (2016). Medium-term self-healing evaluation of engineered cementitious composites with varying amounts of fly ash and exposure durations. *Construction and Building Materials*, 118, 194–203.
- Kang, S. T., Lee, K. S., Choi, J.-I., Lee, Y., FelekogluLee, B., & Bang, Yeon. (2016). Control of tensile behavior of ultra-high performance concrete through artificial flaws and fiber hybridization. *International Journal of Concrete Structures and Materials*, 10(53), 33–41.
- Li, V. C. (2012). Tailoring ECC for special attributes: A review. *International Journal of Concrete Structures and Materials*, 6(3), 135–144.
- Li, V. C., Wang, S., & Wu, C. (2001). Tensile strain-hardening behavior of PVA-ECC. *ACI Materials Journal*, 98(6), 483–492.
- Liu, S., Gu, X. L., & Huang, Q. H. (2008). Experimental study on mechanical properties of steel bars at super-low temperature. *Journal of Building Structures*, 29(s1), 47–51.
- Liu, H. Z., Zhang, Q., Gu, C. S., Su, H. Z., & Li, V. (2017). Self-healing of microcracks in engineered cementitious composites under sulfate and chloride environment. *Construction and Building Materials*, 153, 948–956.
- Maalej, M., & Leong, K. S. (2005). Engineered cementitious composites for effective FRP-strengthening of RC beams. *Composites Science and Technology*, 65(7–8), 1120–1128.
- Maalej, M., & Li, V. C. (1995). Introduction of strain-hardening engineered cementitious composites in design of reinforced concrete flexural members for improved durability. *Structural Journal*, 92(2), 167–176.
- Maalej, M., Quek, S. T., Ahmed, S. F., & Leong, K. S. (2012). Review of potential structural applications of hybrid fiber engineered cementitious composites. *Construction and Building Materials*, 36(11), 216–227.
- Özbay, E., Karahan, O., Lachemi, M., Hossain, K. M., & Atis, C. D. (2013). Dual effectiveness of freezing–thawing and sulfate attack on high-volume slag-incorporated ECC. *Composites Part B: Engineering*, 45(1), 1384–1390.
- Pourfalah, S. (2018). Behaviour of engineered cementitious composites and hybrid engineered cementitious composites at high temperatures. *Construction and Building Materials*, 158, 921–937.
- Qin, X. C., Meng, S. P., Cao, D. F., & Tu, Y. M. (2016). Evaluation of freeze–thaw damage on concrete material and prestressed concrete specimens. *Construction and Building Materials*, 125, 892–904.
- Smarzewski, P., & Barnat-Hunek, D. (2017). Effect of fiber hybridization on durability related properties of ultra-high performance concrete. *International Journal of Concrete Structures and Materials*, 11(2), 315–325.
- Wang, Y. (2017). *Research on mechanical behavior and seismic performance of concrete structure under the freeze–thaw cycles*. Xian: Xi'an University of Architecture and Technology.
- Wu, C., & Li, V. C. (2017). CFRPECC hybrid for strengthening of the concrete structures. *Composite Structures*, 175(15), 372–382.
- Wu, C., Pan, Z., Kim, K. S., & Meng, S. (2017). Theoretical and experimental study of effective shear stiffness of reinforced ECC columns. *International Journal of Concrete Structures and Materials*, 114(4), 585–597.
- Xu, S. L., Cai, X., & Zhang, Y. (2009). Experimental measurement and analysis of the axial compressive stress-strain curve of ultra high toughness cementitious composites. *China Civil Engineering Journal*, 42(11), 79–85.
- Yoo, D. Y., & Yoon, Y.-S. (2016). A review on structural behavior, design, and application of ultra-high-performance fiber-reinforced concrete. *International Journal of Concrete Structures and Materials*, 10(2), 125–142.
- Yuan, F., Pan, J., & Leung, C. K. Y. (2013). Flexural behaviors of ECC and concrete/ECC composite beams reinforced with basalt fiber-reinforced polymer. *Journal of Composites for Construction*, 17(5), 591–602.
- Yun, H.-D., Kim, S. W., Lee, Y. O., Rokugo, K., & Devitt, K. (2011). Tensile behavior of synthetic fiber-reinforced strain-hardening cement-based composite (SHCC) after freezing and thawing exposure. *Cold Regions Science and Technology*, 67(1–2), 49–57.
- Zhang, Y. X. (2014). Simplified method for evaluating the behavior of strain hardening cementitious composite flexural strengthening reinforced concrete members. *Engineering Fracture Mechanics*, 121–122, 11–27.
- Zhang, Y., Ueda, N., Nakamura, H., & Kunieda, Minoru. (2017). Behavior investigation of reinforced concrete members with flexural strengthening using strain-hardening cementitious composite. *ACI Structural Journal*, 114(2), 417–426.
- Zhou, M. H. (2013). *Experiment and test of civil engineering structures* (pp. 113–114). NanJing: Southeast University Press.

Publisher's Note

Springer Nature remains neutral with regard to jurisdictional claims in published maps and institutional affiliations.